


## PAPER

View Article Online  
View Journal | View IssueCite this: *Nanoscale*, 2021, **13**, 15431

# *In situ* synthesis of Fe<sub>2</sub>O<sub>3</sub> nanosphere/Co<sub>3</sub>O<sub>4</sub> nanowire-connected reduced graphene oxide hybrid networks for high-performance supercapacitors†

Yan Wang,<sup>\*a,b</sup> Jianhao Zhou,<sup>a</sup> Zhiyu Zhou,<sup>a</sup> Huifang Lv,<sup>a</sup> Bingni Gu,<sup>c,d,e</sup> Kuangye Wang,<sup>c,d,e</sup> Zexiang Chen,<sup>\*a,b</sup> Xinyu Yan,<sup>a</sup> Jijun Zhang,<sup>a</sup> Wen-Wu Liu<sup>f</sup> and Yu-Lun Chueh<sup>†g</sup> 

Three-dimensional (3D) hybrid networks consisting of reduced graphene oxide (rGO) sheets interconnected by Co<sub>3</sub>O<sub>4</sub> nanowires (rGO/Co<sub>3</sub>O<sub>4</sub>), followed by the decoration of Fe<sub>2</sub>O<sub>3</sub> nanospheres (NSs) (rGO/Co<sub>3</sub>O<sub>4</sub>@Fe<sub>2</sub>O<sub>3</sub>), were demonstrated by a facile hydrothermal method, with which the rGO/Co<sub>3</sub>O<sub>4</sub> networks acted as nucleation sites for the *in situ* synthesis of Fe<sub>2</sub>O<sub>3</sub> NSs. The intimate contacts between rGO, Co<sub>3</sub>O<sub>4</sub> NWs and Fe<sub>2</sub>O<sub>3</sub> NSs, which result in an excellent conductive behavior, provide a unique structure with huge potential for electrochemical property promoted electrochemical supercapacitors. The rGO/Co<sub>3</sub>O<sub>4</sub>@Fe<sub>2</sub>O<sub>3</sub> hybrid networks as electrodes exhibit a high capacitance of 784 F g<sup>-1</sup> at 1 A g<sup>-1</sup> with 83% retention of the initial capacitance as the current density increases from 1 to 10 A g<sup>-1</sup>, which is explained by the graphene-based interconnected structure owing to the advantages of accommodating the volume expansion between Co<sub>3</sub>O<sub>4</sub> NWs and Fe<sub>2</sub>O<sub>3</sub> NSs. The supercapacitor was assembled by applying a nickel aluminum layered double hydroxide (NiAl-LDH) structure and rGO/Co<sub>3</sub>O<sub>4</sub>@Fe<sub>2</sub>O<sub>3</sub> as the electrode materials and yields an energy density of 70.78 W h kg<sup>-1</sup> at a power density of 0.29 kW kg<sup>-1</sup>. The energy density can maintain 24.24 W h kg<sup>-1</sup> with 9.94 kW kg<sup>-1</sup>.

Received 8th January 2021,

Accepted 27th April 2021

DOI: 10.1039/d1nr00126d

rsc.li/nanoscale

## Introduction

Significant advances in materials science have been aided by nanoscience and nanotechnology and have increased many demands for advanced electrochemical energy storage devices

(EESs), such as lithium-ion batteries, alkaline batteries, supercapacitors and traditional lead–acid batteries.<sup>1–3</sup> For conventional electrical double-layer capacitors (EDLCs),<sup>4,5</sup> ions adsorbed (desorbed) at (near) the interface between the electrode material surface and electrolyte contribute to non-faradaic capacitance, which may result in low capacitance. For pseudo-capacitors, the charge can be stored and released in faradaic electron-transfer processes at (near) the interface. Among the above various intelligent devices, notable high power density, efficient recharge capacitance, excellent rate retention and long cycle performance are widely recognized as indispensable features for EESs. Transition metal oxides, especially those with special morphologies or nanostructures, are attractive pseudocapacitive materials for high-performance EESs.<sup>6,7</sup> Among the common metal oxides, Fe<sub>2</sub>O<sub>3</sub>, Co<sub>3</sub>O<sub>4</sub>, CoO, NiO and MnO<sub>2</sub> with their compounds were explored as candidate materials for electrodes due to their excellent physical, chemical and electrochemical properties, such as their high theoretical capacitance, good safety, low cost and good electrochemical performance.<sup>7–10</sup> Because the capability of an electrode material is significantly influenced by the surface area and morphology properties of the materials, an electrode material with a high surface area and uniform, ordered struc-

<sup>a</sup>School of Optoelectronic Science and Engineering of UESTC, University of Electronic Science and Technology of China, Jianshe North Road 4, 610054 Chengdu, China.

E-mail: wangyan127@uestc.edu.cn, zxchen@uestc.edu.cn

<sup>b</sup>Sichuan Province Key Laboratory of Display Science and Technology, Jianshe North Road 4, 610054 Chengdu, China

<sup>c</sup>Department of Materials Science and Engineering, National Tsing Hua University, Hsinchu, 30013, Taiwan. E-mail: ylchueh@mx.nthu.edu.tw

<sup>d</sup>Frontier Research Center on Fundamental and Applied Sciences of Matters, National Tsing Hua University, Hsinchu 30013, Taiwan

<sup>e</sup>Department of Physics, National Sun Yat-Sen University, Kaohsiung, 80424, Taiwan

<sup>f</sup>State Key Laboratory of Advanced Processing and Recycling of Nonferrous Metals, Lanzhou University of Technology, Lanzhou 730050, PR China

†Electronic supplementary information (ESI) available: FTIR spectra of rGO/Co<sub>3</sub>O<sub>4</sub> and rGO/Co<sub>3</sub>O<sub>4</sub>@Fe<sub>2</sub>O<sub>3</sub> samples; photographs of GO and modified rGO; SEM images of rGO/Fe<sub>2</sub>O<sub>3</sub>, Co<sub>3</sub>O<sub>4</sub>/Fe<sub>2</sub>O<sub>3</sub> and the mixture; EDS elemental mapping images of Fe<sub>2</sub>O<sub>3</sub> NS and rGO/Co<sub>3</sub>O<sub>4</sub>@Fe<sub>2</sub>O<sub>3</sub>; charge–discharge curves, rate performance, BET surface areas, Nyquist plots, cycling performances of the rGO/Co<sub>3</sub>O<sub>4</sub> NWs, rGO/Fe<sub>2</sub>O<sub>3</sub> NSs, and rGO/Co<sub>3</sub>O<sub>4</sub>@Fe<sub>2</sub>O<sub>3</sub> mixture. See DOI: 10.1039/d1nr00126d

ture would be expected to exhibit superior performance in a supercapacitor system.

To date, efforts have been made to optimize different aspects, including synthetic strategies, structural diversity and material compositions, to promote the electrochemical properties.<sup>11–15</sup> Qu *et al.* reported a gas bubble-assisted construction of hollow cobalt-based spheres (CoMoO<sub>4</sub>).<sup>16</sup> The obtained hollow spheres facilitate diffusion of KOH electrolyte and greatly decrease the diffusion path, leading to an excellent capacitance of 1381 F g<sup>−1</sup> at 1 A g<sup>−1</sup> and 742 F g<sup>−1</sup> at 10 A g<sup>−1</sup>. The hollow spheres showed outstanding cycling stability when used in supercapacitors. Guan *et al.* reported a facile hydrothermal process to fabricate a hybrid structure, in which the Co<sub>3</sub>O<sub>4</sub> nanowires were decorated on graphene oxide (GO) and the final products with different mass ratios were characterized.<sup>17</sup> The Co<sub>3</sub>O<sub>4</sub>/GO nanocomposites have a strong synergistic effect because of the integration between Co<sub>3</sub>O<sub>4</sub> and GO, leading to an enhanced specific capacitance of 157.7 F g<sup>−1</sup> at 1 A g<sup>−1</sup>, which maintains about 70% after 4000 cycles (0.2 A g<sup>−1</sup>). A morphology modification process can be used to obtain 3D interconnected Fe<sub>2</sub>O<sub>3</sub> nanospheres that have a mean diameter of 10–20 nm. As an electrode, this iron oxide structure delivers improved cycling performance, high rate capability performance, excellent electrochemical properties attributed to the facile transportation of ions and electrons and abundant active sites.<sup>18</sup> However, the obtained capacitance results in the literature are often inferior to theoretical capacitance values because of the huge volume expansion during the redox reaction process and poor electrochemical conductivity. The practical application of Fe<sub>2</sub>O<sub>3</sub>, Co<sub>3</sub>O<sub>4</sub>, or other transition metal oxide-based compounds in energy storage devices is restricted even though the morphology can be easily controlled.<sup>19–22</sup> It requires stable conducting supports to offset their poor electrochemical conductivity, huge mass transfer impedance, insufficient specific surface area and low mechanical stability.<sup>23–25</sup>

Carbon materials that have impressive surface areas are commonly or commercially used as electrode materials for EESs.<sup>26</sup> Graphene is a two-dimensional carbon allotrope widely used to form multiform graphene-based nanostructures and could be a suitable supporting bone/surface due to its superior electrochemical performance and large specific surface area.<sup>27–29</sup> Motivated by the discovery of graphene, scientists have devoted great efforts to integrate nanomaterials with graphene to obtain graphene-supported composite materials.<sup>30,31</sup> Many impressive solutions have been employed to prepare transition metal composites with more than a single component into graphene structures.<sup>32</sup> Transition metal active components integrated with graphene are termed a hybrid capacitor. However, there have been very few studies on the integration of nanowires and nanospheres with graphene layers as hybrid networks, which is a new strategy for graphene-based hybrid architectures. In this regard, we demonstrate the design and preparation of 3D hybrid networks consisting of rGO sheets interconnected by Co<sub>3</sub>O<sub>4</sub> NWs (rGO/Co<sub>3</sub>O<sub>4</sub>), followed by the decoration of Fe<sub>2</sub>O<sub>3</sub> NSs (rGO/

Co<sub>3</sub>O<sub>4</sub>@Fe<sub>2</sub>O<sub>3</sub>) through an *in situ* hydrothermal method, with which the rGO/Co<sub>3</sub>O<sub>4</sub> networks can act as nucleation sites for the following synthesis of Fe<sub>2</sub>O<sub>3</sub> NSs. Fe<sub>2</sub>O<sub>3</sub> has attracted considerable attention because of its environmental sustainability, cost-effectiveness and high theoretical capacitance. In our work, Fe<sub>2</sub>O<sub>3</sub> was chosen as the electrode material due to the increased surface area attributed to the designed nanosize, enabling Fe<sub>2</sub>O<sub>3</sub> to make significant contributions to high capacitance. Cobalt oxides have received more intense attention owing to their high electrical conductivity. Furthermore, tailored techniques have been adopted to obtain Co<sub>3</sub>O<sub>4</sub> NWs, which can connect the bulk unit, thereby enhancing its electrochemical properties. To be more specific, the conductive 1D Co<sub>3</sub>O<sub>4</sub> NWs provide expressways for the transportation of electrons between two separated rGO nanosheets, which considerably link the whole network, yielding enhanced electrical conductivity. Graphene is expected to be a suitable supporting material due to its high electronic conductivity and massive surface area. Thus, it is capable of preventing Co<sub>3</sub>O<sub>4</sub> and Fe<sub>2</sub>O<sub>3</sub> from delivering low power density and poor rate capability. rGO/Co<sub>3</sub>O<sub>4</sub> can also serve as the supporting material for the nucleation growth of Fe<sub>2</sub>O<sub>3</sub> NSs, promoting the conductivity of Fe<sub>2</sub>O<sub>3</sub> NSs and improving the electrochemical performance of the composites simultaneously. Compared with the 1D Co<sub>3</sub>O<sub>4</sub> NWs, the rGO/Co<sub>3</sub>O<sub>4</sub>@Fe<sub>2</sub>O<sub>3</sub> hybrid networks as the electrode material exhibit a much higher specific capacitance of 784 F g<sup>−1</sup> at a current density of 1 A g<sup>−1</sup>. To further investigate the actual capacitance behavior, a supercapacitor, namely a NiAl-LDH//rGO/Co<sub>3</sub>O<sub>4</sub>@Fe<sub>2</sub>O<sub>3</sub> device, was assembled using NiAl-LDH and the optimized rGO/Co<sub>3</sub>O<sub>4</sub>@Fe<sub>2</sub>O<sub>3</sub> hybrid networks as the electrode material, with which an excellent energy density of 70.78 W h kg<sup>−1</sup> at a power density of 0.29 kW kg<sup>−1</sup> can be achieved. Moreover, it can achieve 24.24 W h kg<sup>−1</sup> at 9.94 kW kg<sup>−1</sup> with good cycling stability. The outstanding performances indicate that the rGO/Co<sub>3</sub>O<sub>4</sub>@Fe<sub>2</sub>O<sub>3</sub> hybrid networks are promising negative electrode materials with a 3D electrode configuration in the high-performance supercapacitor.

## Experimental

### Synthesis and thermal reduction of graphite oxide

All of the materials, including CoCl<sub>2</sub>·6H<sub>2</sub>O, FeCl<sub>3</sub>·6H<sub>2</sub>O, urea, NH<sub>4</sub>F, natural graphite, sodium poly(4-styrenesulfonate) (PSS), H<sub>2</sub>SO<sub>4</sub> and ethanol, were purchased and used as received without purification. In our work, rGO was synthesized *via* a modified Hummers' method using natural graphite powders as the reactant. Concentrated H<sub>2</sub>SO<sub>4</sub> was placed in a beaker. Subsequently, the natural graphite powder was then homo-dispersed into the concentrated H<sub>2</sub>SO<sub>4</sub> under magnetic stirring at room temperature. 6 g of KMnO<sub>4</sub> was then added into the above-concentrated H<sub>2</sub>SO<sub>4</sub> under constant magnetic stirring in the reaction beaker. The solution mixture containing the reaction mixture was placed in a water bath at a temperature of 40 °C. Deionized water was then added under vigorous stir-

ring. Finally, 3 mL of  $\text{H}_2\text{O}_2$  (30% aq.) in 100 mL of deionized water was added rapidly into the above mixture. Then, a yellow dispersion can be obtained. The dispersion was washed repeatedly with DI water and dilute HCl solution. The final precipitate was then dispersed in PSS solution to prepare a suspension. The concentrations of the purified GO were determined at around  $1 \text{ mg mL}^{-1}$ . GO solution was exfoliated *via* ultrasonication before each experiment. The solvothermal process was carried out on the rGO/PSS solution at  $200^\circ\text{C}$  for 12 h in order to reduce GO, and the final product was denoted as the rGO/PSS solution.

### Synthesis of the rGO/ $\text{Co}_3\text{O}_4$ precursor

In a typical procedure, 2 mL of  $\text{CoCl}_2 \cdot 6\text{H}_2\text{O}$  aqueous solution ( $0.5 \text{ mol L}^{-1}$ ) was introduced into the rGO/PSS solution under ultrasonication. The mixed solution of urea and  $\text{NH}_4\text{F}$  was then dissolved in 10 mL of ethanol using magnetic stirring. The above solution was magnetically stirred for 10 min, and then the resulting mixed solution was dispersed in the above solution and stirred for another 15 min under continuous magnetic stirring. The above solution was then transferred into a Teflon-lined autoclave and the hydrothermal reaction was conducted at  $200^\circ\text{C}$  and the reaction was continued for 12 h. At the end, the rGO/ $\text{Co}_3\text{O}_4$  precursor sample was collected and washed 3 times with an abundant amount of water. The rGO/ $\text{Co}_3\text{O}_4$  precursor was then kept in PSS solution ( $1 \text{ g L}^{-1}$ ) to prepare a suspension.

### Synthesis of rGO/ $\text{Co}_3\text{O}_4$ @ $\text{Fe}_2\text{O}_3$ hybrid networks

$\text{FeCl}_3 \cdot 6\text{H}_2\text{O}$ , urea and  $\text{NH}_4\text{F}$  were dissolved under vigorous stirring in the rGO/ $\text{Co}_3\text{O}_4$  precursor suspension. Ethanol (10 mL) was added into the above solution for another 15 min to form a homogeneous suspension. When all the components were fully dissolved, the solution was then transferred to a 50 mL autoclave. Then, the hydrothermal reaction was kept at  $200^\circ\text{C}$  and the reaction was continued for 24 h. The solid product was then collected by centrifugation, and washed 3 times with deionized water and ethanol, followed by drying in a vacuum overnight to obtain rGO/ $\text{Co}_3\text{O}_4$ @ $\text{Fe}_2\text{O}_3$  hybrid networks. For comparison, the rGO/ $\text{Fe}_2\text{O}_3$ , rGO/ $\text{Co}_3\text{O}_4$  and  $\text{Fe}_2\text{O}_3$ / $\text{Co}_3\text{O}_4$  solid products were prepared using a similar method with the addition of the corresponding precursor. The simple mixtures of rGO,  $\text{Co}_3\text{O}_4$  and  $\text{Fe}_2\text{O}_3$  were prepared by sonicating the pre-synthesized  $\text{Co}_3\text{O}_4$  and  $\text{Fe}_2\text{O}_3$  with rGO/PSS solution. After that, the suspension was then transferred into a 50 mL autoclave and heated at  $200^\circ\text{C}$  for 24 h. After being cooled to room temperature naturally, the mixtures were then collected by centrifugation.  $\text{Co}_3\text{O}_4$  and  $\text{Fe}_2\text{O}_3$  particles were prepared by sonicating urea,  $\text{NH}_4\text{F}$  and the corresponding chlorides and then conducting the hydrothermal process at  $200^\circ\text{C}$ . The physical mixture of the rGO,  $\text{Co}_3\text{O}_4$  and  $\text{Fe}_2\text{O}_3$  sample is labeled as "Mixture".

### Characterization studies

The phase structures for the samples were examined by X-ray diffraction (XRD) analysis using Cu  $\text{K}\alpha$  radiation with  $\lambda$  of

0.15405 nm. The XRD results were measured at a voltage of 40 kV with 30 mA. Field emission scanning electron microscopy (SEM) and transmission electron microscopy (TEM) were used to investigate the microstructures and compositional properties of the prepared samples. The nitrogen adsorption/desorption isotherms were performed on a micromeritics ASAP 2010 absorptiometer, which was measured at a liquid nitrogen temperature of  $-196^\circ\text{C}$ . The specific surface area was calculated using the Brunauer-Emmett-Teller (BET) method. Electrochemical performance tests for the materials were investigated on an automatic electrochemical testing system (RST 5200). Pt foil was used as the counter electrode and  $\text{Hg}/\text{HgO}$  was used as the reference electrode. The working electrode was prepared by mixing the active materials, conductive additives and binders in a ratio of 80 : 15 : 5 to form a mixture and then coated onto a piece of nickel foam ( $10 \times 10 \text{ mm}$ ). The mass loading of the electrode materials is controlled to about  $10 \text{ mg cm}^{-2}$ . Finally, the fabricated electrode was pressed as a slice under a pressure of 15 MPa. The cyclic voltammetric (CV) measurements, galvanostatic charge-discharge (GCD) tests, and electrochemical impedance spectroscopy (EIS) measurements were performed to evaluate the electrochemical behaviors for the obtained samples. The specific capacitance of the electrode was determined from the GCD cycles. The assembled supercapacitor ( $\text{NiAl-LDH}/\text{rGO}/\text{Co}_3\text{O}_4/\text{Fe}_2\text{O}_3$ ) used NiAl-LDH and rGO/ $\text{Co}_3\text{O}_4$ @ $\text{Fe}_2\text{O}_3$  as the electrode materials. To optimize the charges between NiAl-LDH and rGO/ $\text{Co}_3\text{O}_4$ @ $\text{Fe}_2\text{O}_3$  electrodes, the mass was balanced using the equation:  $m_+/m_- = C_s - \Delta V_- / C_s + \Delta V_+$ , where  $m$  is the material mass,  $C_s$  is the specific capacitances of the electrodes and  $\Delta V$  is the voltage range.

## Results and discussion

To identify the phases and structures of the rGO/ $\text{Co}_3\text{O}_4$ @ $\text{Fe}_2\text{O}_3$  hybrid networks, the XRD results of GO, rGO, rGO/ $\text{Co}_3\text{O}_4$ , rGO/ $\text{Fe}_2\text{O}_3$  and rGO/ $\text{Co}_3\text{O}_4$ @ $\text{Fe}_2\text{O}_3$  were measured as shown in Fig. 1(a). A characteristic peak, which is located at  $\sim 9.9^\circ$  can be assigned to GO. Compared with pure  $\text{Co}_3\text{O}_4$ , the major diffraction peaks of the rGO/ $\text{Co}_3\text{O}_4$  hybrid networks are almost unchanged, indicating that the high purity of  $\text{Co}_3\text{O}_4$  NWs can be well maintained within the 3D interconnected rGO/ $\text{Co}_3\text{O}_4$  hybrid networks. The typical features of rGO layers were also observed by SEM and TEM. According to XRD results, the characteristic peaks of  $\text{Co}_3\text{O}_4$  and  $\text{Fe}_2\text{O}_3$  matched well with the spinel cobalt oxide and hematite ferric oxide, respectively. Besides, the major diffractions in the hybrid networks are almost unchanged, indicating that the particle phase in the hybrid networks can be well maintained. For the rGO/ $\text{Co}_3\text{O}_4$ @ $\text{Fe}_2\text{O}_3$  hybrid networks, the characteristic  $\text{Co}_3\text{O}_4$  peaks at  $31.2^\circ$ ,  $36.8^\circ$  and  $65.2^\circ$  were found, demonstrating the successful preparation of the high purity  $\text{Co}_3\text{O}_4$  crystal. Besides, the  $\text{Fe}_2\text{O}_3$  peaks at  $33.1^\circ$ ,  $35.6^\circ$  and  $54.1^\circ$ , corresponding to the (104), (110) and (116) planes, prove the existence of  $\text{Fe}_2\text{O}_3$  NSs on the surface of rGO nanosheets. Moreover, the characteristic



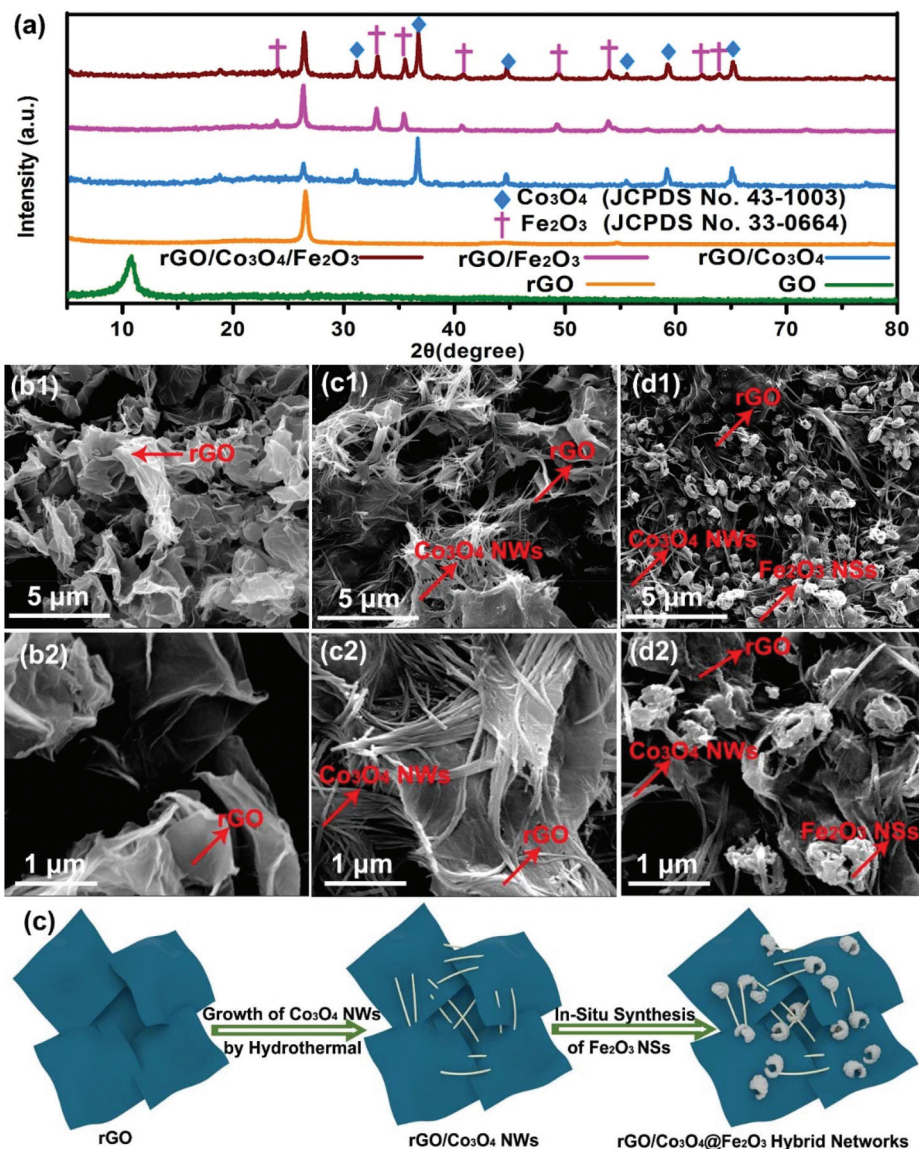


**Fig. 1** (a) XRD results of GO, rGO/Co<sub>3</sub>O<sub>4</sub> NWs, rGO/Fe<sub>2</sub>O<sub>3</sub> NSs and rGO/Co<sub>3</sub>O<sub>4</sub>@Fe<sub>2</sub>O<sub>3</sub> hybrid networks. SEM images of GO (b1–b2), rGO/Co<sub>3</sub>O<sub>4</sub> (c1–c2) and rGO/Co<sub>3</sub>O<sub>4</sub>@Fe<sub>2</sub>O<sub>3</sub> (d1–d2). The insets in b2, c2 and d2 are the schematic diagrams of the corresponding morphologies. (c) Schematic of the formation for rGO/Co<sub>3</sub>O<sub>4</sub>@Fe<sub>2</sub>O<sub>3</sub> hybrid networks.

peak of rGO at around  $26^\circ$  could be ascribed to the (002) plane. For the rGO/Co<sub>3</sub>O<sub>4</sub>@Fe<sub>2</sub>O<sub>3</sub> sample, the peak at  $26^\circ$  can be indexed to the (002) plane of the rGO nanosheets. Employing rGO nanosheets as the supporting bones in hybrid networks, the coexistence of Co<sub>3</sub>O<sub>4</sub> NWs and Fe<sub>2</sub>O<sub>3</sub> NSs on the surface confirms the synthesis of rGO/Co<sub>3</sub>O<sub>4</sub>@Fe<sub>2</sub>O<sub>3</sub> hybrid networks. The FTIR spectra of the as-prepared rGO/Co<sub>3</sub>O<sub>4</sub> and rGO/Co<sub>3</sub>O<sub>4</sub>@Fe<sub>2</sub>O<sub>3</sub> samples are shown in Fig. S1 in the ESI.† The characteristic peak at around  $3520\text{ cm}^{-1}$  was attributed to O–H bending and stretching modes of water molecules from solvents in two samples, respectively. The peak at  $\sim 1720\text{ cm}^{-1}$  corresponds to the vibrations of C=O groups, and  $\sim 1525\text{ cm}^{-1}$  to C=C of rGO, suggesting that the partially reduced graphene can be obtained. In addition, the relatively weak peaks at

$\sim 1120\text{ cm}^{-1}$  correspond to the functional group of C–O–C. Two strong absorption bands at  $665$  and  $562\text{ cm}^{-1}$  in the rGO/Co<sub>3</sub>O<sub>4</sub> sample were assigned to Co–O stretching and bending vibration modes of Co<sub>3</sub>O<sub>4</sub>, respectively. On the other hand, the integration of Co<sub>3</sub>O<sub>4</sub> and Fe<sub>2</sub>O<sub>3</sub> particles on rGO sheets can be confirmed from the low region (in the range of  $750\text{--}500\text{ cm}^{-1}$ ), marked by a circle. Therefore, XRD results and FTIR spectra confirm that rGO/Co<sub>3</sub>O<sub>4</sub> and rGO/Co<sub>3</sub>O<sub>4</sub>@Fe<sub>2</sub>O<sub>3</sub> samples can be successfully synthesized. Fig. S2(a) and S2(b)† show the photographic images of GO and PSS-modified-rGO suspensions. After modification with different surfactants and reduction processes at the desired temperature of  $200^\circ\text{C}$ , the yellow-brown exfoliated-GO suspension turned black. It is because the exposed hydrophilic groups on the surface of the

GO layers were removed, which is attributed to the deoxygenation of GO nanosheets in a thermal environment, yielding the synthesis of rGO nanosheets. Note that the reduction of GO nanosheets efficiently prevents graphene-based hybrid networks from aggregating. The SEM images of the rGO nanosheets as shown in Fig. 1(b1) and (b2) confirm a typical sheet structure with crumples that have an average planar size of 1–5  $\mu\text{m}$  and the corresponding cartoon image of rGO nanosheets is schematically illustrated in Fig. 1(c). Note that rGO nanosheets can attain a large surface area with enhanced electrical conductivity, which eliminates the need for conductive fillers, leading to more efficient electrodes. Hair-like  $\text{Co}_3\text{O}_4$  NWs as shown in Fig. 1(c1) and (c2) were uniformly grown throughout the networks of the surface-modified-rGO nanosheets by the *in situ* hydrothermal method. As a result, the rGO/ $\text{Co}_3\text{O}_4$  hybrid networks consist of 2D rGO building blocks that are interconnected by  $\text{Co}_3\text{O}_4$  NWs, with which numerous mass transfer channels can be formed throughout the 3D conductive hybrid networks. In addition, the SEM images as shown in Fig. 1(d1) and (d2) reveal that  $\text{Fe}_2\text{O}_3$  NSs (diameters ranging from hundreds of nanometers to microns) were closely grown throughout the interconnected rGO/ $\text{Co}_3\text{O}_4$  hybrid networks. Note that the SEM image of rGO/ $\text{Co}_3\text{O}_4$ @ $\text{Fe}_2\text{O}_3$  is similar to that of the rGO/ $\text{Co}_3\text{O}_4$  hybrid networks, confirming that the *in situ* hydrothermal process used in the current study to synthesize  $\text{Fe}_2\text{O}_3$  NSs does not damage the structure of the  $\text{Co}_3\text{O}_4$  NWs. Specifically,  $\text{Fe}_2\text{O}_3$  NSs can only be formed on the surface of the  $\text{Co}_3\text{O}_4$  NWs on the rGO nanosheets as the rGO/ $\text{Co}_3\text{O}_4$ @ $\text{Fe}_2\text{O}_3$  hybrid networks. Decoration of  $\text{Fe}_2\text{O}_3$  NSs on the rGO/ $\text{Co}_3\text{O}_4$  hybrid networks promoted the electrical conductivity of  $\text{Fe}_2\text{O}_3$  NSs. The rGO/ $\text{Co}_3\text{O}_4$ @ $\text{Fe}_2\text{O}_3$  hybrid networks feature unique topological connectivity and electrical conductivity. The networks are suitable for potential use as positive electrode materials in supercapacitors. For comparison,  $\text{Fe}_2\text{O}_3$  NSs were also directly integrated with rGO (rGO/ $\text{Fe}_2\text{O}_3$ ), with which nanostructures of the transition metal compounds were constructed on the surface of rGO nanosheets as shown in Fig. S3.† Note that morphologies and structures of nano-units on the rGO/ $\text{Fe}_2\text{O}_3$  hybrid networks can be changed by selecting the  $\text{Fe}(\text{NO}_3)_3$  precursor as the reactant, showing irregularly shaped and grape-like  $\text{Fe}_2\text{O}_3$  NSs with an average diameter of about  $\sim 400$  nm decorated on the rGO surface. Moreover,  $\text{Co}_3\text{O}_4$  and  $\text{Fe}_2\text{O}_3$  without the addition of GO (labeled as  $\text{Co}_3\text{O}_4/\text{Fe}_2\text{O}_3$ ) were also obtained by a similar process in order to provide evidence of the importance of graphene. Fig. S4† shows that the  $\text{Co}_3\text{O}_4$  NWs are  $\sim 50$  nm and a few microns in diameter and length, respectively.  $\text{Fe}_2\text{O}_3$  NSs have diameters of  $\sim 50$ – $600$  nm. Close inspection of the  $\text{Co}_3\text{O}_4/\text{Fe}_2\text{O}_3$  product shows that  $\text{Co}_3\text{O}_4$  NWs and  $\text{Fe}_2\text{O}_3$  NSs are just loosely attached to each other, confirming a simple mechanically mixed structure, in which  $\text{Co}_3\text{O}_4$  nanowires and  $\text{Fe}_2\text{O}_3$  nanospheres co-existed. The SEM images of the Mixture are shown in Fig. S5.† The rGO,  $\text{Co}_3\text{O}_4$  and  $\text{Fe}_2\text{O}_3$  components are attached to each other irregularly, demonstrating a simple mechanical mixture property. To sum up, the incorporation of  $\text{Co}_3\text{O}_4$  NWs and  $\text{Fe}_2\text{O}_3$  NSs into the

rGO sheets has advantages over the single component of the abovementioned rGO/ $\text{Co}_3\text{O}_4$  and rGO/ $\text{Fe}_2\text{O}_3$  hybrid networks. The rGO/ $\text{Co}_3\text{O}_4$ @ $\text{Fe}_2\text{O}_3$  hybrid networks, which contain both  $\text{Co}_3\text{O}_4$  and  $\text{Fe}_2\text{O}_3$  components, offer richer redox reactions than rGO/ $\text{Co}_3\text{O}_4$  and rGO/ $\text{Fe}_2\text{O}_3$  hybrid networks. The  $\text{Fe}_2\text{O}_3$  NSs have attractive properties such as high voltage window, which are conducive to promoting the electrochemical capacitance. The excellent mechanical stability of the  $\text{Fe}_2\text{O}_3$  NSs can effectively relieve the volume collapse/expansion during redox reaction processes, leading to the enhanced cycle life. The rGO nanosheets are covered with numerous  $\text{Co}_3\text{O}_4$  NWs, leading to excellent conductivity and abundant open spaces from interconnected hybrid networks that are beneficial for the infiltration of the electrolyte, facilitating rapid ionic diffusion. These unique interconnected hybrid networks enable electrolyte ions to follow rapid channels to the surfaces for the application of the pseudocapacitive materials with short mass (electrons and ions) diffusion paths, resulting in faster kinetics and higher rate capability. In addition, both  $\text{Co}_3\text{O}_4$  NWs and  $\text{Fe}_2\text{O}_3$  NSs are nanostructures, which greatly expand the specific surface area, endowing the rGO/ $\text{Co}_3\text{O}_4$ @ $\text{Fe}_2\text{O}_3$  hybrid networks with high electrochemical performance.

A schematic diagram of the strategy for the *in situ* preparation of the rGO/ $\text{Co}_3\text{O}_4$ @ $\text{Fe}_2\text{O}_3$  hybrid networks is shown in Fig. 1(c). The conductive  $\text{Co}_3\text{O}_4$  NWs and  $\text{Fe}_2\text{O}_3$  NSs grown on rGO nanosheets were fabricated by the *in situ* hydrothermal method with multistep processes simultaneously (see Experimental procedures for more details). GO was first modified *via* a thermal reduction method, and PSS surfactants, including hydroxyl, sulfonic, carbonyl and carboxyl functional groups, were all introduced onto the surface of the rGO layers. Thus, the modified rGO/ $\text{H}_2\text{O}$  solution exhibits a good dispersion behavior in an aqueous solution, which can efficiently prevent the irreversible agglomeration of rGO. Note that rGO/ $\text{H}_2\text{O}$  solution confers a large negative charge triggered by reactive hydroxyl, sulfonic and carboxylic acid groups on the rGO nanosheets. Typically, ultrasonication and stirring were used to first mix  $\text{CoCl}_2 \cdot 6\text{H}_2\text{O}$  with the rGO aqueous dispersion. 3D interconnected  $\text{Co}_3\text{O}_4$  NWs decorated on the rGO layers were realized by the hydrothermal method, in which rGO nanosheets act as supporting bones. During the hydrothermal process, PSS was used as a soft template to form the nanowires.  $\text{Co}_2^{+}$  ions preferentially anchor on the oxygen-containing groups of the surface-treated rGO nanosheets, which can serve as the nucleation active sites to anchor  $\text{Co}_3\text{O}_4$  NWs. Because of the cooperative decomposition of  $\text{NH}_4\text{F}$  and pyrolyzation of urea during the hydrothermal reaction, liberated hydroxide ions and carbonate ions form an alkaline environment at high temperature, which is beneficial for the generation of  $\text{Co}_3\text{O}_4$  seed monomers. These  $\text{Co}_3\text{O}_4$  primary particles precipitated as nuclei and quickly grew into the primary particles directly on the rGO nanosheets along with the PSS molecular chain template, yielding a large area in the rGO/ $\text{Co}_3\text{O}_4$  hybrid networks. The composite consisting of 3D rGO/ $\text{Co}_3\text{O}_4$  networks was used as the nucleation sites to graft  $\text{Fe}_2\text{O}_3$  NSs, the typical structure possessing active centers, hollow spaces and enlarged specific

surface area.  $\text{Fe}^{3+}$  first reacted in an alkaline environment, and it precipitated as nuclei and quickly grew into the primary particles. PSS polymers acted as a template to control the morphologies of  $\text{Fe}_2\text{O}_3$  materials. In the system, there are large complex micelles on graphene/ $\text{Co}_3\text{O}_4$ , which are assembled by PSS micelles and produce polyanions with a strong ability to interact with electropositive active sites in water. Because the aggregation cores might distribute on graphene/ $\text{Co}_3\text{O}_4$  substrates along different directions, the as-formed  $\text{Fe}_2\text{O}_3$  NSs were intersected, producing core-shell structures. The resulting 3D structure can be termed  $\text{rGO}/\text{Co}_3\text{O}_4@\text{Fe}_2\text{O}_3$  hybrid networks, which represent a designed 3D nanostructure containing synergistic effects derived from each component. Note that in the symbol “/” indicates that  $\text{Co}_3\text{O}_4$  NWs go throughout the entire rGO nanosheets, while “@” means that  $\text{Fe}_2\text{O}_3$  NSs are dispersed and decorated on  $\text{rGO}/\text{Co}_3\text{O}_4$  hybrid networks after the *in situ* synthesis process. Specifically, our  $\text{rGO}/\text{Co}_3\text{O}_4@\text{Fe}_2\text{O}_3$  hybrid networks integrate the following important features as a positive electrode: (1)  $\text{Co}_3\text{O}_4$  NWs provide interconnected bridges for electrolyte infiltration out of the electrode, which is favorable for the rapid transfer/diffusion of the electrolyte. (2)  $\text{Co}_3\text{O}_4$  NWs on rGO nanosheets act as highly conductive paths for charge transportation, which can connect two large rGO nanosheets to establish an electronic transmission bridge, resulting in the high electrical conductivity of the interconnected hybrid networks. (3) The highly dispersed  $\text{Fe}_2\text{O}_3$  NSs because of the *in situ* hydrothermal process with the intimate contacts to the  $\text{rGO}/\text{Co}_3\text{O}_4$  hybrid networks possess distinct features compared with other hybrid compounds from mechanical mixing methods. These uniformly distributed  $\text{Fe}_2\text{O}_3$  NSs throughout the networks feature characteristics including highly capacitive and relatively high electrical conductivity, which is beneficial for mass transport during the redox reaction. Therefore, our optimized configuration simultaneously addresses key issues, including mechanical stability, electrochemical capacitance and dispersibility of the particles with great potential to substantially promote the electrochemical property.

TEM results were used to investigate the detailed microstructures of  $\text{rGO}/\text{Co}_3\text{O}_4@\text{Fe}_2\text{O}_3$  hybrid networks. Fig. 2(a) and (b) show that the entire surface of the rGO nanosheets was uniformly wrapped in or connected by  $\text{Co}_3\text{O}_4$  NWs and  $\text{Fe}_2\text{O}_3$  NSs, for which the interconnected networks of  $\text{Co}_3\text{O}_4$  NWs and  $\text{Fe}_2\text{O}_3$  NSs on the surface of the rGO nanosheets, constructing a 3D hybrid network, can be confirmed. We can see that  $\text{Fe}_2\text{O}_3$  NSs (~400 nm) are distributed uniformly throughout the whole  $\text{rGO}/\text{Co}_3\text{O}_4$  hybrid networks, and the interconnected networks can be well preserved over the entire experimental procedures, including the *in situ* method. The reason can be explained by the relatively stable *in situ* decoration of  $\text{Fe}_2\text{O}_3$  NSs with strong adhesion to the  $\text{rGO}/\text{Co}_3\text{O}_4$  surfaces within the 3D structure where almost every  $\text{Fe}_2\text{O}_3$  NS is entangled by multiple  $\text{Co}_3\text{O}_4$  NWs from different orientations. This unique connection between the different components creates a 3D interconnected nanostructure material with good mechanical stability. In the high magnification TEM image as shown in Fig. 2(c) and (d), the  $\text{Co}_3\text{O}_4$  NWs possess properties such as

thin walls, a large radius and smooth surface, where the diameters for the  $\text{Co}_3\text{O}_4$  NWs can be ~30 to 50 nm with lengths of a few micrometers. Acting as the bridge between  $\text{Fe}_2\text{O}_3$  NS centers and rGO nanosheets in the  $\text{rGO}/\text{Co}_3\text{O}_4@\text{Fe}_2\text{O}_3$  hybrid networks,  $\text{Co}_3\text{O}_4$  NWs ensure the growth of abundant tiny  $\text{Fe}_2\text{O}_3$  crystal seeds during the *in situ* process where the highly dispersed  $\text{Fe}_2\text{O}_3$  NSs on the networks can be obtained by controlling the process parameters. The selected area electron diffraction (SAED) measurement was also used to further determine the crystal information. As shown in the inset in Fig. 2(c), the calculated lattice spacing based on R1–R3 confirms (111), (220) and (311) planes of the  $\text{Co}_3\text{O}_4$  phase, revealing the presence of  $\text{Co}_3\text{O}_4$  NWs in the hybrid networks. A magnified TEM image of a single  $\text{Co}_3\text{O}_4$  NW shows uniform contrast also demonstrating their nanowire nature. The corresponding HRTEM image as shown in the inset of Fig. 2(d) reveals the single crystalline feature. The lattice spacing was found to be 0.234 nm, corresponding to the (400) crystal planes for spinel-type  $\text{Co}_3\text{O}_4$ . A SAED pattern as shown in the upper inset in Fig. 2(e) confirms hematite-type  $\text{Fe}_2\text{O}_3$ . In addition, two planes in the HRTEM image as shown in Fig. 2(e) were indexed to be of 0.27 and 0.23 nm, corresponding to the (104) and (006) crystal planes of the hematite-type  $\text{Fe}_2\text{O}_3$ , respectively. EDS elemental mapping images in Fig. S6† demonstrate the uniform distribution of Fe and O in  $\text{Fe}_2\text{O}_3$  NS. Fig. 2(f) shows the typical TEM image that the  $\text{Co}_3\text{O}_4$  NWs and  $\text{Fe}_2\text{O}_3$  NSs were closely joined together. Obviously, each  $\text{Fe}_2\text{O}_3$  NS has been infiltrated by  $\text{Co}_3\text{O}_4$  NWs, leading to a tight connection. As a result, a large number of uniformly dispersed  $\text{Fe}_2\text{O}_3$  NSs with  $\text{Co}_3\text{O}_4$  NW bridges by *in situ* growth is the key advantage in our  $\text{rGO}/\text{Co}_3\text{O}_4@\text{Fe}_2\text{O}_3$  hybrid networks, which significantly enhances the electrochemistry effect. Besides, the EDS elemental mapping images of  $\text{rGO}/\text{Co}_3\text{O}_4@\text{Fe}_2\text{O}_3$  hybrid networks (Fig. S7†) reveal the spatial elemental distribution within the interconnected network where the homogeneous spatial distribution of C, O, Fe and Co mapping images was obtained, respectively. The quantitative EDS results were also used to confirm the composition of  $\text{rGO}/\text{Co}_3\text{O}_4@\text{Fe}_2\text{O}_3$ , for which the atomic ratio for Fe:Co:C:O inside  $\text{rGO}/\text{Co}_3\text{O}_4@\text{Fe}_2\text{O}_3$  hybrid networks can be found to be 1:1.65:4.33:3.86. As a result, all material characterization results confirm typical heterojunctions between  $\text{rGO}/\text{Co}_3\text{O}_4/\text{Fe}_2\text{O}_3$  during the crystal growth process on the surface of rGO nanosheets.

The intimate contact between these heterojunctions accounts for fast mass (electron and ions) transfer within the electrode during redox reactions and is beneficial for the infiltration of electrolyte, thereby ensuring better electrochemical performance. To evaluate the electrochemical performance of the as-synthesized hybrid networks, we used a three-electrode system to characterize the electrochemical performance. The  $\text{rGO}/\text{Co}_3\text{O}_4@\text{Fe}_2\text{O}_3$  electrode was then tested using CV measurements in a potassium hydroxide electrolyte (6 M) at a scan rate of 5  $\text{mV s}^{-1}$ . For comparison, the electrochemical results of  $\text{rGO}/\text{Co}_3\text{O}_4$ ,  $\text{rGO}/\text{Fe}_2\text{O}_3$  and the Mixture were also measured. The CV curves of electrodes were first recorded at a scan rate of 5  $\text{mV s}^{-1}$  for 10 cycles to decrease the polarization



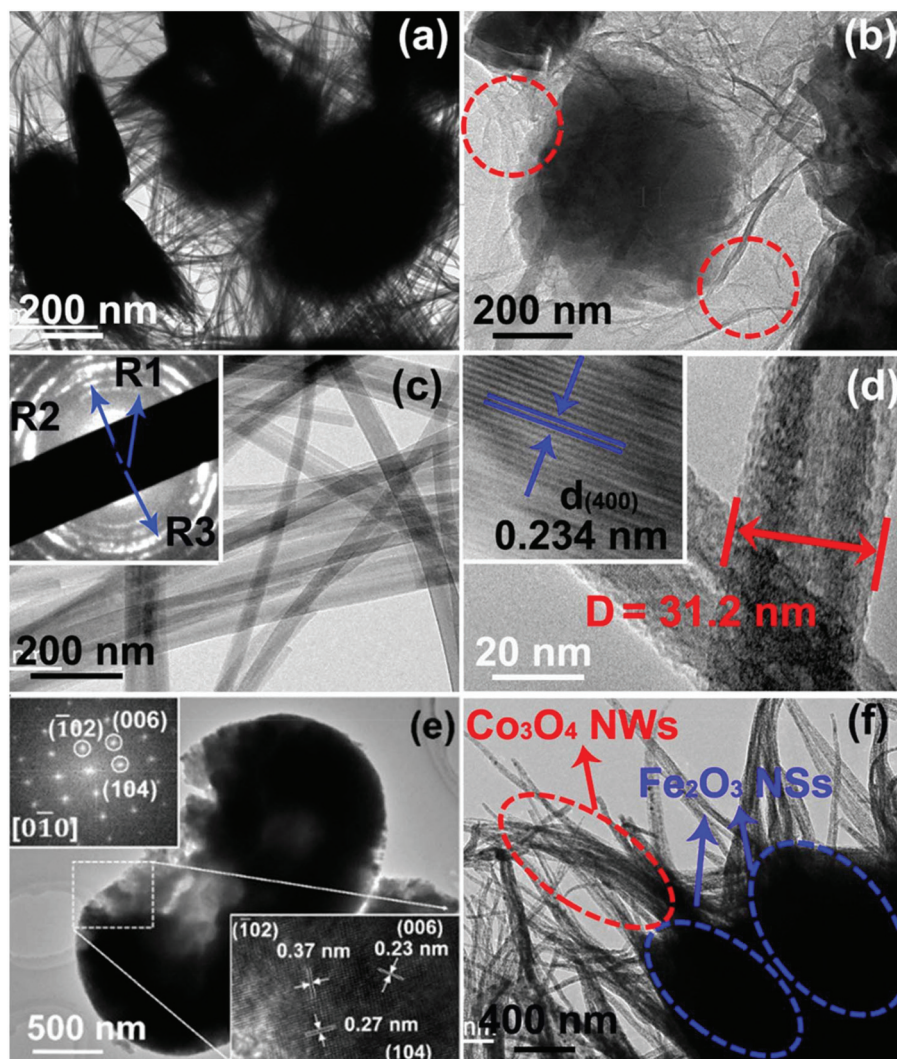
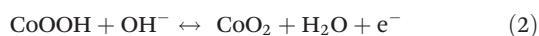
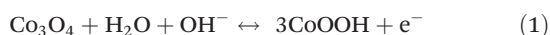


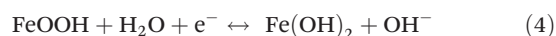
**Fig. 2** TEM images of rGO/Co<sub>3</sub>O<sub>4</sub>@Fe<sub>2</sub>O<sub>3</sub> hybrid networks. (a) and (b) TEM results of the rGO/Co<sub>3</sub>O<sub>4</sub>@Fe<sub>2</sub>O<sub>3</sub> hybrid networks. (c) and (d) TEM results of Co<sub>3</sub>O<sub>4</sub> NWs. The insets in (c) and (d) show the SAED for the Co<sub>3</sub>O<sub>4</sub> NWs and the HRTEM image for the Co<sub>3</sub>O<sub>4</sub> NW region. (e) TEM results for Fe<sub>2</sub>O<sub>3</sub> NSs. The inset in (e) shows the SAED for the Fe<sub>2</sub>O<sub>3</sub> NS region. (f) TEM results of the Co<sub>3</sub>O<sub>4</sub> NW and Fe<sub>2</sub>O<sub>3</sub> NS interconnected region in the hybrid networks.

effect of the active materials and to stabilize the reaction system as much as possible. Considering the charge passed by integrating the area under the CV measurements, the CV results of rGO/Co<sub>3</sub>O<sub>4</sub>@Fe<sub>2</sub>O<sub>3</sub> are much higher than those of rGO/Co<sub>3</sub>O<sub>4</sub>, rGO/Fe<sub>2</sub>O<sub>3</sub> and the Mixture, indicating that the capacitance of the rGO/Co<sub>3</sub>O<sub>4</sub>@Fe<sub>2</sub>O<sub>3</sub> electrode is the highest among three composites. Fig. 3(a) shows a pair of redox peaks in each of the CV results, indicating the battery-type characteristics of electrodes. For rGO/Co<sub>3</sub>O<sub>4</sub>, the redox couples are ascribed to conversion between Co<sub>3</sub>O<sub>4</sub>, CoOOH and CoO<sub>2</sub>, which can be simply expressed by:



At the lower potential region, the redox reaction should be related to the Co<sup>2+</sup>/Co<sup>3+</sup> system. In contrast, at the higher

potential region, before the oxygen evolution phenomenon, the Co<sup>3+</sup>/Co<sup>4+</sup> system should be dominant.<sup>33</sup> The redox couple in rGO/Fe<sub>2</sub>O<sub>3</sub> can be ascribed to another plausible redox reaction of Fe<sub>2</sub>O<sub>3</sub>, FeOOH and Fe(OH)<sub>2</sub>, which occurs near −0.56 V in the KOH electrolyte by:



For the rGO/Co<sub>3</sub>O<sub>4</sub>@Fe<sub>2</sub>O<sub>3</sub> composite and the Mixture, the redox reactions that occurred at the rGO/Co<sub>3</sub>O<sub>4</sub>@Fe<sub>2</sub>O<sub>3</sub> electrode from −0.5 to −0.8 V are attributed to the conversion of Co<sub>3</sub>O<sub>4</sub> and Fe<sub>2</sub>O<sub>3</sub>, respectively. However, the two anodic and cathodic peaks can hardly be distinguished because of the two contiguous anodic and cathodic peaks, which are ascribed to the synergistic effect between Co<sub>3</sub>O<sub>4</sub> and Fe<sub>2</sub>O<sub>3</sub> materials.<sup>34</sup>

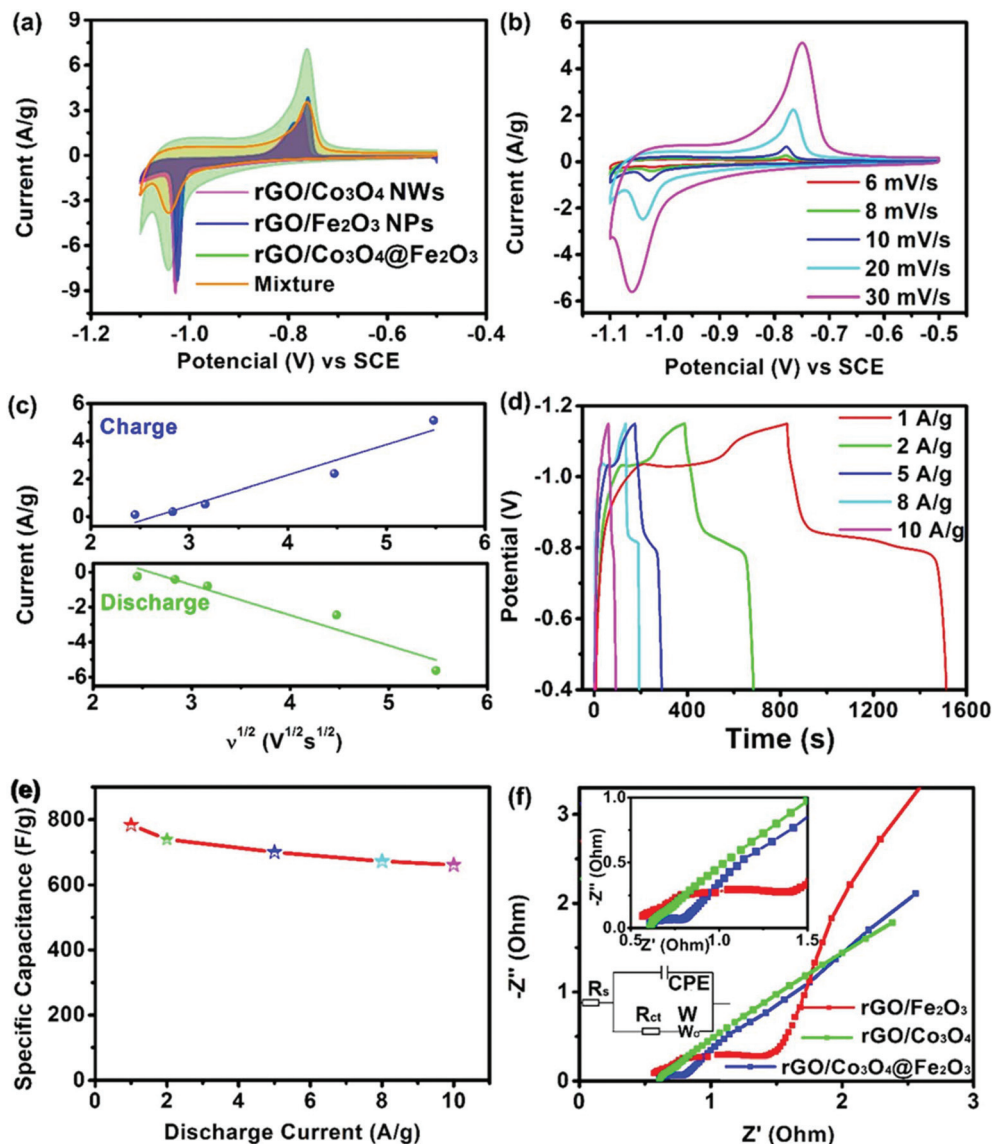


**Fig. 3** (a) CV testing results of the rGO/Co<sub>3</sub>O<sub>4</sub> NW, rGO/Fe<sub>2</sub>O<sub>3</sub> NS and rGO/Co<sub>3</sub>O<sub>4</sub>@Fe<sub>2</sub>O<sub>3</sub> hybrid networks measured at 5 mV s<sup>-1</sup>. (b) CV testing results of the rGO/Co<sub>3</sub>O<sub>4</sub>@Fe<sub>2</sub>O<sub>3</sub> hybrid networks measured from 5 to 20 mV s<sup>-1</sup>. (c) Relationship illustration of the peak currents and the  $v^{1/2}$  for the rGO/Co<sub>3</sub>O<sub>4</sub>@Fe<sub>2</sub>O<sub>3</sub> hybrid network electrode. Discharge curves (d) of the rGO/Co<sub>3</sub>O<sub>4</sub>@Fe<sub>2</sub>O<sub>3</sub> hybrid networks. The calculated capacitance (e) of the rGO/Co<sub>3</sub>O<sub>4</sub>@Fe<sub>2</sub>O<sub>3</sub> hybrid networks. (f) EIS testing results of the rGO/Co<sub>3</sub>O<sub>4</sub> NW, rGO/Fe<sub>2</sub>O<sub>3</sub> NS and rGO/Co<sub>3</sub>O<sub>4</sub>@Fe<sub>2</sub>O<sub>3</sub> hybrid networks.

The improved electrochemical property of rGO/Co<sub>3</sub>O<sub>4</sub>@Fe<sub>2</sub>O<sub>3</sub> is attributed to a synergistic coupling co-effect among rGO, Co<sub>3</sub>O<sub>4</sub> and Fe<sub>2</sub>O<sub>3</sub> in the designed structure in which a simple physical mixture of different components can hardly achieve such high capacitance.<sup>35</sup> The synergistic coupling effect can efficiently decrease the mass transfer distance and transfer impedance, resulting in the enlarged surface area and the exposed active sites as well as the rapid electrochemical reaction, thereby facilitating the improved electrochemical performance. The CV behaviors of the rGO/Co<sub>3</sub>O<sub>4</sub>@Fe<sub>2</sub>O<sub>3</sub> electrode in the KOH electrolyte (6 M) were further investigated. Fig. 3(b) shows the CV curves at different scan rates where an increase in peak current for the redox reaction as the scan rate

increases can be confirmed. Note that the shape of the curve is almost identical to the original shape, indicating the rapid electron transfer kinetics within the rGO/Co<sub>3</sub>O<sub>4</sub>@Fe<sub>2</sub>O<sub>3</sub> electrode because of the low resistance owing to the improved conductivity of the rGO/Co<sub>3</sub>O<sub>4</sub>@Fe<sub>2</sub>O<sub>3</sub> networks. Thus, the rGO/Co<sub>3</sub>O<sub>4</sub>@Fe<sub>2</sub>O<sub>3</sub> electrode can undergo high current density tests. To decide the effects of the Ni foam substrate, CV results for nickel foam were recorded. However, it can be ignored because the intensity of the signal is weak. Fig. 3(c) shows the linear relationship between the peak current and the scan rates. The peak current linearly increases with the square root of the scan rates within all the tested scan rates, indicating that the fast electrochemical redox reaction for the rGO/



Co<sub>3</sub>O<sub>4</sub>@Fe<sub>2</sub>O<sub>3</sub> hybrid network is dominated by the diffusion-controlled process. Notably, the electron storage mechanism depends on the diffusion-controlled behavior not only on the surface of the material but also in the bulk of the electrode. Therefore, a much higher specific capacitance can be obtained, which is attributed to the adsorption of ions and the redox reaction on/near the surface of the electrode. GCD curves of the rGO/Co<sub>3</sub>O<sub>4</sub>@Fe<sub>2</sub>O<sub>3</sub> from 1 to 10 A g<sup>-1</sup> were recorded as shown in Fig. 3(d). All of the tested curves depict that the charge–discharge curves have quasi-rectangular shapes with almost identical voltage plateaus, which match well with the above CV results. Our specific capacitance at different discharge current densities was calculated using the following equation:  $C_{sp} = \frac{It}{mV}$ , where  $C_{sp}$  represents the calculated specific capacitance,  $I$  represents the discharge current,  $t$  represents the discharge time,  $V$  represents the potential range upon discharging and  $m$  represents the mass of the active materials. Fig. 3(e) shows the calculated specific capacitance values for the electrode. At a relatively low current density (1.0 A g<sup>-1</sup>), the rGO/Co<sub>3</sub>O<sub>4</sub>@Fe<sub>2</sub>O<sub>3</sub> hybrid network exhibits a high capacitance of 784 F g<sup>-1</sup>, and even when the current density is as high as 10 A g<sup>-1</sup>, the rGO/Co<sub>3</sub>O<sub>4</sub>@Fe<sub>2</sub>O<sub>3</sub> hybrid network still maintains the high capacitance of 661 F g<sup>-1</sup>, suggesting that 84.3% of the capacitance remains as the current increases 10 times. As the scan rate increases, the movement of ions is restricted by insufficient diffusion, and electrolyte ions are not available for the interior surfaces of the whole material because of the reduced mass diffusion time. Only the active surface was used for the electrochemical reaction, resulting in the decreased specific capacitance. Fig. S8† shows the GCD curves and the rate abilities of rGO/Co<sub>3</sub>O<sub>4</sub>, rGO/Fe<sub>2</sub>O<sub>3</sub>, Mixture and rGO/Co<sub>3</sub>O<sub>4</sub>@Fe<sub>2</sub>O<sub>3</sub> at 1.0 A g<sup>-1</sup>. Clearly, for the fixed current density, rGO/Co<sub>3</sub>O<sub>4</sub>@Fe<sub>2</sub>O<sub>3</sub> hybrid networks exhibit a longer discharge time than rGO/Co<sub>3</sub>O<sub>4</sub>, the Mixture or rGO/Fe<sub>2</sub>O<sub>3</sub> because of the improved capacitance and the results are consistent with the CV tests. Note that the nickel foam does not make an obvious contribution to the total capacitance. The rGO/Co<sub>3</sub>O<sub>4</sub> hybrid networks provide a remarkable specific capacitance of 672.3 F g<sup>-1</sup> at 1 A g<sup>-1</sup> and then the capacitance decreases to 58.3% as the current density increases to 10 A g<sup>-1</sup>. The rGO/Fe<sub>2</sub>O<sub>3</sub> hybrid networks deliver a capacitance of 728.8 F g<sup>-1</sup> at 1 A g<sup>-1</sup>, which drops to 61.5% when the current density increases to 10 A g<sup>-1</sup>. Moreover, the Mixture provides a specific capacitance of 700.6 F g<sup>-1</sup> at 1 A g<sup>-1</sup> and then the capacitance decreases to 51.4% as the current density increases to 10 A g<sup>-1</sup>. The increase in electrochemical capacitance and promoted rate capability of the rGO/Co<sub>3</sub>O<sub>4</sub>@Fe<sub>2</sub>O<sub>3</sub> network can be ascribed to the unique interconnected conductive network nanostructures that exhibit more abundant reaction sites, good electrical conductivity and short mass (electron and ions) diffusion length. BET surface areas of the three prepared samples were tested as shown in Fig. S9,† where the surface area of rGO/Co<sub>3</sub>O<sub>4</sub>@Fe<sub>2</sub>O<sub>3</sub> was found to be 165 m<sup>2</sup> g<sup>-1</sup>. The BET surface area of rGO/Co<sub>3</sub>O<sub>4</sub>@Fe<sub>2</sub>O<sub>3</sub> is larger than that of either rGO/Co<sub>3</sub>O<sub>4</sub> (154.5 m<sup>2</sup> g<sup>-1</sup>) or rGO/Fe<sub>2</sub>O<sub>3</sub> (147.7 m<sup>2</sup> g<sup>-1</sup>), which can supply more active areas for the redox reaction.

Furthermore, the close contact within the interconnected network can ensure an electron transport highway for the fast electrochemical redox reaction, especially at high rates. Nyquist plots of rGO/Co<sub>3</sub>O<sub>4</sub>, rGO/Fe<sub>2</sub>O<sub>3</sub> and rGO/Co<sub>3</sub>O<sub>4</sub>@Fe<sub>2</sub>O<sub>3</sub> are presented in Fig. 3(f). The program Zview was used to fit the EIS results. An equivalent circuit model was used with the Zview software as shown in the bottom inset in Fig. 3(f). Nyquist plots are basically composed of a semicircle and a straight line. A larger semicircle at the high-frequency region indicates the larger charge-transfer resistance and a higher slope signifies the lower diffusion rate. At the high-frequency region, an intercept with the real axis is attributed to the ohmic resistance of the electrode. The semicircle at the high-frequency region corresponds to the charge transfer resistance ( $R_{ct}$ ), while the slope of the curve at the low-frequency region represents the Warburg impedance. As a result, the  $R_s$  value of rGO/Co<sub>3</sub>O<sub>4</sub>, rGO/Fe<sub>2</sub>O<sub>3</sub> and rGO/Co<sub>3</sub>O<sub>4</sub>@Fe<sub>2</sub>O<sub>3</sub> electrodes was 0.43, 0.78 and 0.47  $\Omega$ , respectively. The rGO/Co<sub>3</sub>O<sub>4</sub> and the rGO/Co<sub>3</sub>O<sub>4</sub>@Fe<sub>2</sub>O<sub>3</sub> hybrid networks have lower  $R_s$  values than rGO/Fe<sub>2</sub>O<sub>3</sub>, which is attributed to the excellent incorporation between the Co<sub>3</sub>O<sub>4</sub> NWs and the rGO nanosheets in the hybrid networks. Nyquist plots of rGO/Co<sub>3</sub>O<sub>4</sub> and rGO/Co<sub>3</sub>O<sub>4</sub>@Fe<sub>2</sub>O<sub>3</sub> electrodes at the high-frequency region exhibit a smaller semicircle than that of the rGO/Fe<sub>2</sub>O<sub>3</sub> electrode due to the lower interfacial charge transfer resistance. A more vertical line can be found in the rGO/Fe<sub>2</sub>O<sub>3</sub> electrode at the low-frequency region, which indicates that the ions are more easily adsorbed by the electrode surface and are more easily diffused into the active materials. The slopes of the lines indicate that the rGO/Fe<sub>2</sub>O<sub>3</sub> electrode delivers lower ionic diffusion resistance than the rGO/Co<sub>3</sub>O<sub>4</sub> and the rGO/Co<sub>3</sub>O<sub>4</sub>@Fe<sub>2</sub>O<sub>3</sub> electrodes. The lower ionic diffusion resistance for the rGO/Fe<sub>2</sub>O<sub>3</sub> electrode due to the uniformly decorated Fe<sub>2</sub>O<sub>3</sub> on graphene can indicate the close contact between the interface and electrolyte. However, the slopes of the lines at the lower-frequency region (<1.5) or higher-frequency regions (>2.2) show the small difference. Low impedance benefits high performance, so more innovative efforts should be devoted to lower the impedance of the composite. Moreover, the electrochemical performance of the electrode is determined by multi-factors, such as the crystal structure, morphologies, stability and electrical conductivity. Comprehensive electrochemical performance depends on the balance of various factors.

Furthermore, typical impedance spectra of the rGO/Co<sub>3</sub>O<sub>4</sub>@Fe<sub>2</sub>O<sub>3</sub> electrode at various cycles were recorded as shown in Fig. S10.† After the 10<sup>th</sup> and 20<sup>th</sup> cycles, the interfacial charge transfer resistance gradually decreases. The decrease in interfacial charge transfer resistance can be attributed to the infiltration of electrolytes throughout the electrode, leading to an increase in the available active sites within the composites that enhance contact and reduce mass (electrons and ions) transfer length. The increased available interfacial area can result in reduced resistance because of the material/electrolyte interface. Consequently, the lower resistance designates the rapid charge transfer rate of ions in the electrolyte, which indicates the better redox reaction properties of the electrode. As a result, the  $R_{ct}$  value gradually decreases throughout

the cycling because of an activation process, which is consistent with the tendency of the cycling performance, implying a faster charge transfer process. After 100 cycles, the  $R_{ct}$  value of the rGO/Co<sub>3</sub>O<sub>4</sub>@Fe<sub>2</sub>O<sub>3</sub> remains stable without any considerable change, with which a steady process after a certain activation can be achieved. This is why the rGO/Co<sub>3</sub>O<sub>4</sub>@Fe<sub>2</sub>O<sub>3</sub> hybrid network exhibits improved electrical conductivity with low charge-diffusion resistance. Based on the above results, the excellent electrochemical performance of the rGO/Co<sub>3</sub>O<sub>4</sub>@Fe<sub>2</sub>O<sub>3</sub> can be attributed to the unique stable structure and surface properties: (i) the nano-structure uniformly confined with nanowires and nanospheres with a large surface area can ensure a high weight fraction of active components, shorten the diffusion length and accelerate the mass-transfer kinetics, resulting in the improvement of mass transport and the enhancement of redox reaction kinetics. (ii) The Fe<sub>2</sub>O<sub>3</sub> integrated on graphene is chemically self-assembled with a mechanically stable interface. After the Co<sub>3</sub>O<sub>4</sub> connection process, the rGO/Co<sub>3</sub>O<sub>4</sub>@Fe<sub>2</sub>O<sub>3</sub> composite can rebuild the microstructures by creating additional electric channels resulting in the composite with improved electrochemical performance. (iii) The strong synergistic interaction among rGO, Co<sub>3</sub>O<sub>4</sub> and Fe<sub>2</sub>O<sub>3</sub> ensures superior structural stability, effectively suppressing volume changes during electrochemical processes, leading to improved electron transfer with high rate capability. Specifically, the characteristics of the rGO/Co<sub>3</sub>O<sub>4</sub>@Fe<sub>2</sub>O<sub>3</sub> hybrid networks, including the larger active surface area and faster mass and electron transfer, synergistically deliver superior electrochemical performance.

To further demonstrate the potential application of the rGO/Co<sub>3</sub>O<sub>4</sub>@Fe<sub>2</sub>O<sub>3</sub> hybrid networks for energy storage devices, a supercapacitor was assembled using NiAl-LDH as the cathode, the rGO/Co<sub>3</sub>O<sub>4</sub>@Fe<sub>2</sub>O<sub>3</sub> hybrid networks as the anode and 6 M KOH solution as the electrolyte. The CV results of NiAl-LDH//rGO/Co<sub>3</sub>O<sub>4</sub>@Fe<sub>2</sub>O<sub>3</sub> were investigated at different scan rates as shown in Fig. 4(a). Each CV curve in Fig. 4(a) shows a pair of redox peaks, which indicates the battery-type characteristics of NiAl-LDH//rGO/Co<sub>3</sub>O<sub>4</sub>@Fe<sub>2</sub>O<sub>3</sub> devices. In addition, CV curves clearly show that the peak current of the electrochemical redox reaction increases as the scan rate increases. Note that the curve almost retains its original shape, indicating that the electron transfer kinetics of the electrochemical redox reactions on the device are relatively fast. Fig. 4(b) shows the dependence of the anodic and cathodic peak current at different scan rates under charge and discharge processes. The anodic and cathodic peak current increases linearly with respect to the square root of the scan rate. The observed linear relationship between the peak current values and  $\nu^{1/2}$  suggests that the electrodes have a pseudocapacitive nature, which is limited by the diffusion of ions to the active sites. To further prove the capacitive behavior, the electrode kinetics were investigated to analyze the contribution of the capacitance. Normally, two types of surface process capacitances in electrode materials can be found, including capacitance contributed by redox reactions and

capacitance *via* reversible charge stored by an electric double layer. The capacitance includes redox reactions that take place at active sites, while the diffusion-controlled capacitance occurs from the bulk materials. Specifically, scan-rate-dependent CV curves recorded from 0.25 mV s<sup>-1</sup> to 1.00 mV s<sup>-1</sup> in the voltage range from 0 to 1.65 V as shown in Fig. 4(c) were measured to quantify the charge contribution by the surface capacitive effect or the diffusion-controlled processes to the total stored charge given by  $I(V) = k_1\nu + k_2\nu^{1/2}$ , where  $I(V)$  is the total current response at a certain potential  $V$ . The value  $k_1\nu$  represents the current response due to the surface capacitive effects and  $k_2\nu^{1/2}$  represents the current response because of the diffusion-controlled process. As a result,  $I(V)/\nu^{1/2}$  vs.  $\nu^{1/2}$  can be plotted at different potentials. The corresponding slope and intercept can be calculated from the straight lines to distinguish two types of processes as shown in Fig. 4(d). When the charge was applied at a low scan rate of 0.25 mV s<sup>-1</sup>, 25% of the total capacitance can be determined to be a capacitive effect, indicating that the charge storage behavior can be dominated by the ionic diffusion process as shown in Fig. 4(e). In addition, the contribution ratio at different scan rates was measured to distinguish the dominant charge process as shown in Fig. 4(f). As the scanning rate increases, the diffusion contribution can be depressed. The capacitive contribution can reach a maximum value of 75.5% at a high scan rate of 1.0 mV s<sup>-1</sup>. At a scan rate of 1.0 mV s<sup>-1</sup>, the capacitance contribution was dominated by the capacitive behavior. Therefore, the increase in the capacitive storage stemmed from the interconnected rGO/Co<sub>3</sub>O<sub>4</sub>@Fe<sub>2</sub>O<sub>3</sub> hybrid network that can improve the reactivity of active sites and the efficiency of the charge collection. The findings indicate that the rGO/Co<sub>3</sub>O<sub>4</sub>@Fe<sub>2</sub>O<sub>3</sub> hybrid networks provide large capacitive contribution with excellent rate performance because of mesoporous structures.

Furthermore, the charge-discharge curves of the device are shown in Fig. 5(a). A high specific capacitance of 212 F g<sup>-1</sup> was achieved at 1 A g<sup>-1</sup> for the device and a specific capacitance of 154.7 F g<sup>-1</sup> still remains at 50 A g<sup>-1</sup>. The device delivers a capacitance retention of 72.9% as the current density increases 50 times, exhibiting ultrahigh rate capability. For practical applications, the energy and power densities were calculated from the GCD results using  $E = \int IV dt = \Delta V \times \frac{I}{m} \times t$  and  $P = \frac{E}{t} = \Delta V \times \frac{I}{m}$ , where  $I$  is the charge/discharge current (A),  $V$  is the potential window,  $t$  is the discharge time (s) and  $m$  is the total mass of both the cathode and anode active materials. As a result, the NiAl-LDH//rGO/Co<sub>3</sub>O<sub>4</sub>@Fe<sub>2</sub>O<sub>3</sub> supercapacitor yields a high energy density of 70.78 W h kg<sup>-1</sup> at a power density of 0.29 kW kg<sup>-1</sup> and still maintains an energy density of 24.24 W h kg<sup>-1</sup> at a high power density of 9.94 kW kg<sup>-1</sup> from Ragone plots as shown in Fig. 5(b), which are comparable to other Ni/Co/Fe-based cells and devices, such as 3D PMNC/G-2//AC (41 W h kg<sup>-1</sup> at a power density of 216 W kg<sup>-1</sup> and a power density of 4200 W kg<sup>-1</sup> at an energy density of 29.3 W h kg<sup>-1</sup>),<sup>36</sup> NiCo<sub>2</sub>O<sub>4</sub>/NiO/Fe<sub>2</sub>O<sub>3</sub> (19 W h kg<sup>-1</sup> at a power density of 157 W kg<sup>-1</sup>),<sup>37</sup> Ni<sub>3</sub>(PO<sub>4</sub>)<sub>2</sub>@RGO// $\alpha$ -Fe<sub>2</sub>O<sub>3</sub>@GO (67.2 W h kg<sup>-1</sup> at a power density of 200.43 W kg<sup>-1</sup>),<sup>38</sup> CoNi@SNC//AC (15.9 W h

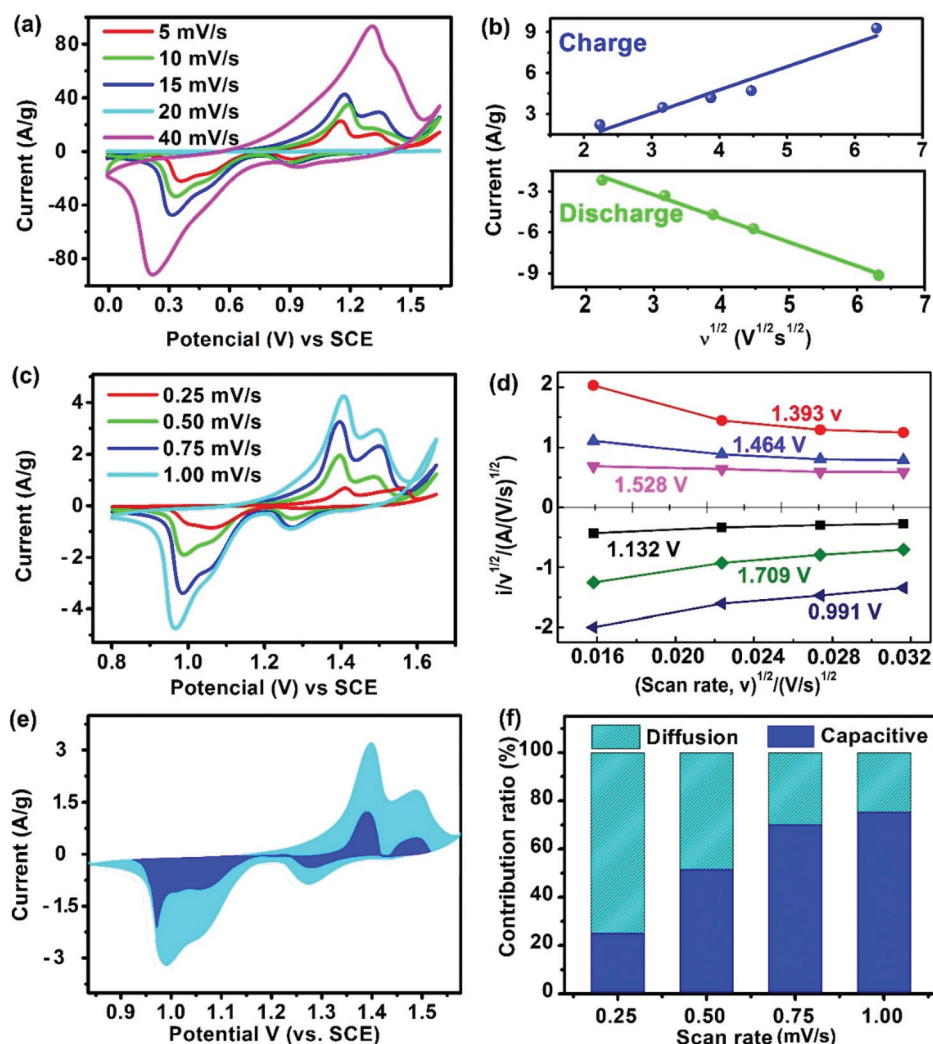


**Fig. 4** (a) CV testing results of the NiAl-LDH/rGO/Co<sub>3</sub>O<sub>4</sub>@Fe<sub>2</sub>O<sub>3</sub> supercapacitor from 5 to 40 mV s<sup>-1</sup>. (b) Relationship illustration of the peak currents and the  $v^{1/2}$  for the NiAl-LDH/rGO/Co<sub>3</sub>O<sub>4</sub>@Fe<sub>2</sub>O<sub>3</sub> supercapacitor. (c) CV testing results of the NiAl-LDH/rGO/Co<sub>3</sub>O<sub>4</sub>@Fe<sub>2</sub>O<sub>3</sub> supercapacitor from 0.25 to 1.00 mV s<sup>-1</sup>. (d) Relationship illustration of  $v^{1/2}$  and  $i/v^{1/2}$ , the calculated  $k_1$  and  $k_2$  values were collected. (e) Charge storage contributions to the electrochemical capacitance at 0.75 mV s<sup>-1</sup>. (f) Contribution ratios of the electrochemical capacitance of the NiAl-LDH/rGO/Co<sub>3</sub>O<sub>4</sub>@Fe<sub>2</sub>O<sub>3</sub> supercapacitor.

kg<sup>-1</sup> at a power density of 120 W kg<sup>-1</sup>),<sup>39</sup> NiCo<sub>2</sub>O<sub>4</sub>/NGN/CNTs//NGN/CNTs (42.7 W h kg<sup>-1</sup> at a power density of 775 W kg<sup>-1</sup>),<sup>40</sup> and CC@NiCo<sub>2</sub>O<sub>4</sub>//CC@NC (31.9 W h kg<sup>-1</sup> at a power density of 2.9 kW kg<sup>-1</sup>, and maintaining 27.3 W h kg<sup>-1</sup> at a power density of 22.9 kW kg<sup>-1</sup>).<sup>41</sup> The rGO/Co<sub>3</sub>O<sub>4</sub>@Fe<sub>2</sub>O<sub>3</sub> composite material is a potentially important material and this work may provide an effective way in the design of other Ni/Co/Fe-based materials. Besides, this structure has been compared with other graphene-based anode materials. More graphene-based composites including Fe-Co-S/GNF,<sup>42</sup> Mn-Zn-Fe-O/G-ink,<sup>43</sup> RGO/Mn<sub>3</sub>O<sub>4</sub>,<sup>44</sup> Fe<sub>3</sub>O<sub>4</sub>@PGNs<sup>45</sup> and Fe<sub>2</sub>O<sub>3</sub>/rGO<sup>46</sup> have been studied. Table S1† shows the comparison of energy density, power density or specific capacitance of these RGO-based composites, which were specifically used as the anode materials in supercapacitors or alkaline batteries. The values indicate that our composites achieved better capacitance compared to RGO/

Mn<sub>3</sub>O<sub>4</sub>, Fe<sub>3</sub>O<sub>4</sub>@PGNs and Fe<sub>2</sub>O<sub>3</sub>/rGO materials, and almost equivalent values to Fe-Co-S/GNF and Mn-Zn-Fe-O/G-ink. Due to the fact that the active carbon or carbon based materials were usually used as the anode materials, the low capacitance may hinder the further development of the energy storage devices. Thus, composite materials of graphene and metal oxides are potentially important materials for high-performance anode materials. Diverse synthetic methods and innovative structures may provide solutions to the high-performance composite. Moreover, the cycling performance of our supercapacitor was measured at 1 A g<sup>-1</sup> within the potential window of 0 to 1.65 V for 1000 cycles as shown in Fig. 5(c). After 1000 cycles, a capacitance retention of 84.7% still remains, confirming the high stability of the supercapacitor. Distinctly, the cycling performance of the supercapacitor is higher than that of the devices assembled using rGO/Co<sub>3</sub>O<sub>4</sub>,



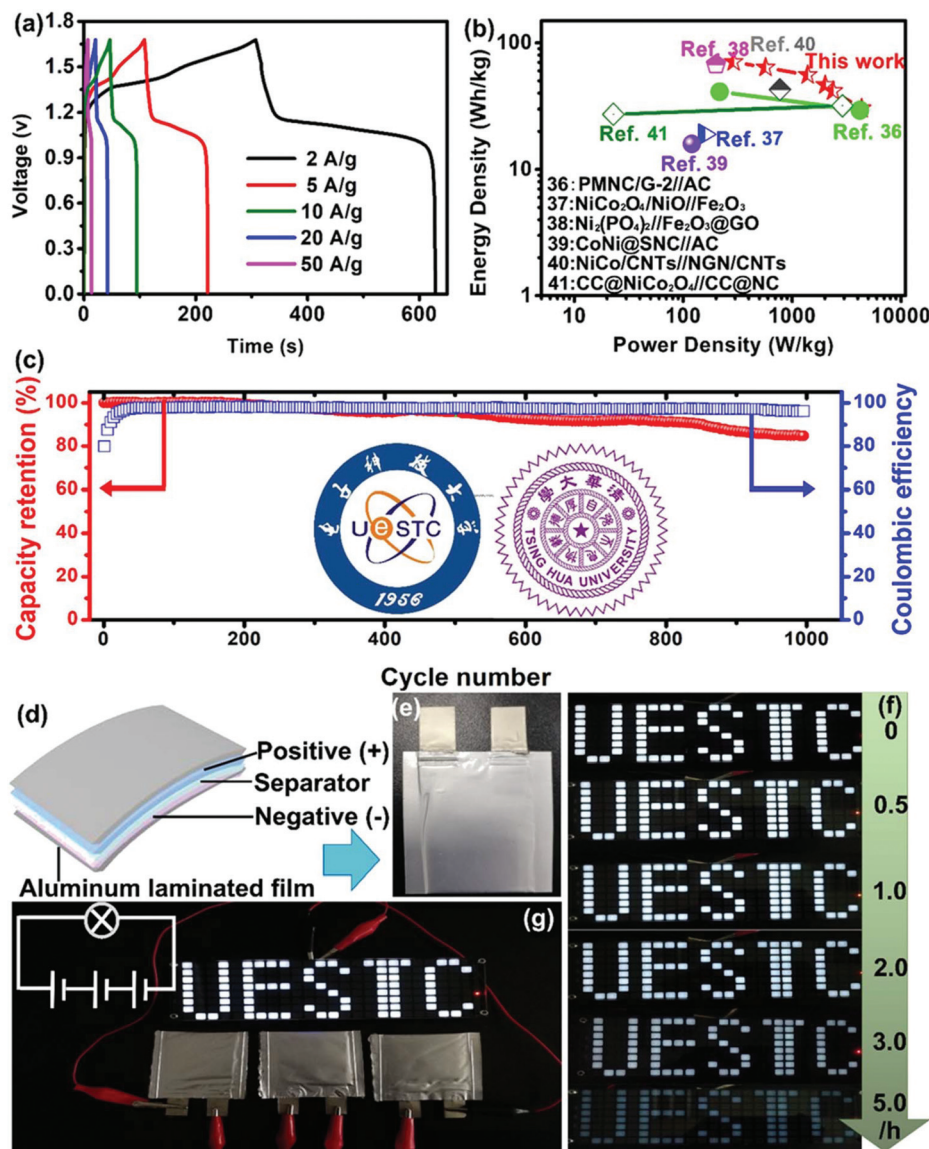


**Fig. 5** (a) GCD testing results of the NiAl-LDH//rGO/Co<sub>3</sub>O<sub>4</sub>@Fe<sub>2</sub>O<sub>3</sub> supercapacitor. (b) Ragone plots of the assembled NiAl-LDH//rGO/Co<sub>3</sub>O<sub>4</sub>@Fe<sub>2</sub>O<sub>3</sub> supercapacitor in comparison with those of the reported literature. (c) Cycling life testing of the NiAl-LDH//rGO/Co<sub>3</sub>O<sub>4</sub>@Fe<sub>2</sub>O<sub>3</sub> devices at 1.0 A g<sup>-1</sup> and the corresponding coulombic efficiency of the NiAl-LDH//rGO/Co<sub>3</sub>O<sub>4</sub>@Fe<sub>2</sub>O<sub>3</sub> device. (d) Schematic diagrams of the morphology of the NiAl-LDH//rGO/Co<sub>3</sub>O<sub>4</sub>@Fe<sub>2</sub>O<sub>3</sub> device. (e) Photograph of the assembled NiAl-LDH//rGO/Co<sub>3</sub>O<sub>4</sub>@Fe<sub>2</sub>O<sub>3</sub> device. (f) Different stages of powering the LEDs using NiAl-LDH//rGO/Co<sub>3</sub>O<sub>4</sub>@Fe<sub>2</sub>O<sub>3</sub> devices. (g) The NiAl-LDH//rGO/Co<sub>3</sub>O<sub>4</sub>@Fe<sub>2</sub>O<sub>3</sub> supercapacitor connected to power LEDs.

rGO/Fe<sub>2</sub>O<sub>3</sub> or Mixture hybrid network as the anode materials and NiAl-LDH as the cathode material which were denoted as NiAl-LDH//rGO/Co<sub>3</sub>O<sub>4</sub>, NiAl-LDH//rGO@Fe<sub>2</sub>O<sub>3</sub> and NiAl-LDH//Mixture, respectively. The corresponding capacitance retentions are 72.5%, 66.4% and 52.6% measured after 1000 cycles, respectively, as shown in Fig. S11.† The excellent cycle life can be explained by the rGO-based nanostructure owing to the advantages of accommodating the volume expansion of Co<sub>3</sub>O<sub>4</sub> NWs and Fe<sub>2</sub>O<sub>3</sub> NSs in rGO nanosheets with the reduced electrochemical impedance during cycling processes. Besides, the good thermal and mechanical stabilities of the interconnected rGO/Co<sub>3</sub>O<sub>4</sub>@Fe<sub>2</sub>O<sub>3</sub> hybrid networks can improve the

utilization rate and maintain the structural stability. This is why the high stability of the NiAl-LDH//rGO/Co<sub>3</sub>O<sub>4</sub>@Fe<sub>2</sub>O<sub>3</sub> device can withstand a long-term cycling behavior toward the feasibility of constructing advanced aqueous supercapacitors. Furthermore, the excellent mechanical and electrical properties of rGO/Co<sub>3</sub>O<sub>4</sub>@Fe<sub>2</sub>O<sub>3</sub> hybrid networks are highly desirable in packed portable devices. To shed light on this part, a schematic diagram of the device is shown in Fig. 5(d), wherein the NiAl-LDH//rGO/Co<sub>3</sub>O<sub>4</sub>@Fe<sub>2</sub>O<sub>3</sub> supercapacitor was assembled by sandwiching a Celgard separator between rGO/Co<sub>3</sub>O<sub>4</sub>@Fe<sub>2</sub>O<sub>3</sub> and NiAl-LDH. The device was prepared to evaluate the practical application as shown in Fig. 5(e). It can

be connected in series or parallel to control the assembly of the potential window and the energy storage capacitance. When these device modules were connected in three series, a high voltage of about 3.5 V can be achieved as shown in Fig. 5(g), which is highly capable of powering a group of light emitting diodes (LEDs) for at least 5 h as shown in Fig. 5(f), suggesting the potential of using the device in a light weight power supply of portable devices.

## Conclusions

In summary, the synthesis of three-dimensional (3D) hybrid networks consisting of rGO nanosheets interconnected by  $\text{Co}_3\text{O}_4$  NWs ( $\text{rGO}/\text{Co}_3\text{O}_4$ ), followed by *in situ* decoration of  $\text{Fe}_2\text{O}_3$  NSs ( $\text{rGO}/\text{Co}_3\text{O}_4@\text{Fe}_2\text{O}_3$ ) was carried out through the hydrothermal method, with which the  $\text{rGO}/\text{Co}_3\text{O}_4$  networks acted as nucleation sites for the following growth of  $\text{Fe}_2\text{O}_3$  NSs. The  $\text{rGO}/\text{Co}_3\text{O}_4@\text{Fe}_2\text{O}_3$  hybrid networks exhibit excellent electrochemical performance. Note that the conductive 1D  $\text{Co}_3\text{O}_4$  NWs provide expressways for the transportation of electrons between two separated rGO nanosheets, which considerably link the whole networks, yielding the enhanced electrical conductivity. The  $\text{rGO}/\text{Co}_3\text{O}_4$  can also serve as a supporting material for the loading of  $\text{Fe}_2\text{O}_3$  NSs, promoting the conductivity of  $\text{Fe}_2\text{O}_3$  NSs and improving the electrochemical performance of the hybrid networks, simultaneously. As an electrode material for an energy storage device, the  $\text{rGO}/\text{Co}_3\text{O}_4@\text{Fe}_2\text{O}_3$  hybrid networks exhibit a superior capacitance of  $784 \text{ F g}^{-1}$  at a current density of  $1 \text{ A g}^{-1}$  in 6 M KOH solution. Furthermore, the NiAl-LDH and the  $\text{rGO}/\text{Co}_3\text{O}_4@\text{Fe}_2\text{O}_3$  were used as the positive electrode and as the negative electrode, respectively, demonstrating the practicality of  $\text{rGO}/\text{Co}_3\text{O}_4@\text{Fe}_2\text{O}_3$  in a supercapacitor. The assembled ASC device delivers a high energy density of  $70.78 \text{ W h kg}^{-1}$  at a power density of  $0.29 \text{ kW kg}^{-1}$  and still maintains an energy density of  $24.24 \text{ W h kg}^{-1}$  at a high-power density of  $9.94 \text{ kW kg}^{-1}$ . Therefore, the findings demonstrate an essential strategy for balancing capacitance and rate stability using the  $\text{rGO}/\text{Co}_3\text{O}_4@\text{Fe}_2\text{O}_3$  heterostructure, and it can be used in future work.

## Conflicts of interest

There are no conflicts to declare.

## Acknowledgements

This work is based upon financial support from the National Natural Science Foundation of China (NSFC 51702037 and 61704021). The research is also supported by the Ministry of Science and Technology through grant No. 107-2923-E-007-002-MY3, 107-2218-E-007-055-, 108-2218-E-007-045-, 107-2112-M-007 -030-MY3 and 109-2634-F-007-023. This work was also sponsored by the Sichuan Province Key Laboratory of Display

Science and Technology. Y. L. Chueh appreciates the use of the facility at CNMM.

## Notes and references

- 1 L. Hu, C. Dai, H. Liu, Y. Li, B. Shen, Y. Chen, S.-J. Bao and M. Xu, *Adv. Energy Mater.*, 2018, **8**, 1800709.
- 2 C. Guan, W. Zhao, Y. Hu, Q. Ke, X. Li, H. Zhang and J. Wang, *Adv. Energy Mater.*, 2016, **6**, 1601034.
- 3 L. Zhang, D. Shi, T. Liu, M. Jaroniec and J. Yu, *Mater. Today*, 2019, **25**, 35–65.
- 4 P. Kulkarni, S. K. Nataraj, R. G. Balakrishna, D. H. Nagaraju and M. V. Reddy, *J. Mater. Chem. A*, 2017, **5**, 22040–22094.
- 5 Q. Yun, Q. Lu, X. Zhang, C. Tan and H. Zhang, *Angew. Chem., Int. Ed.*, 2018, **57**, 626–646.
- 6 Y. Ouyang, R. Huang, X. Xia, H. Ye, X. Jiao, L. Wang, W. Lei and Q. Hao, *Chem. Eng. J.*, 2019, **355**, 416–427.
- 7 X. Cao, J. He, H. Li, L. Kang, X. He, J. Sun, R. Jiang, H. Xu, Z. Lei and Z.-H. Liu, *Small*, 2018, **14**, 1800998.
- 8 Z. Zhou, Q. Zhang, J. Sun, B. He, J. Guo, Q. Li, C. Li, L. Xie and Y. Yao, *ACS Nano*, 2018, **12**, 9333–9341.
- 9 Y. Song, X. Lu, P. Deng, W. Hu, Z. Sun, X.-X. Liu and X. Sun, *Chem. Eng. J.*, 2018, **354**, 672–679.
- 10 L. Ye, L. Zhao, H. Zhang, P. Zan, S. Gen, W. Shi, B. Han, H. Sun, X. Yang and T. Xu, *J. Mater. Chem. A*, 2017, **5**, 1603–1613.
- 11 H. Pang, X. R. Li, Q. X. Zhao, H. G. Xue, W. Y. Lai, Z. Hu and W. Huang, *Nano Energy*, 2017, **35**, 138–145.
- 12 N. Sikdar, B. Konkena, J. Masa, W. Schuhmann and T. K. Maji, *Chem. – Eur. J.*, 2017, **23**, 18049–18056.
- 13 W. Shi, F. Guo, C. Zhu, H. Wang, H. Li, H. Huang, Y. Liu and Z. Kang, *J. Mater. Chem. A*, 2017, **5**, 19800–19807.
- 14 Y. Zhou, Y. Wu, P. Zhang, J. Chen, B. Qu and J.-T. Li, *ACS Appl. Mater. Interfaces*, 2017, **9**, 30880–30890.
- 15 H. Yan, J. Bai, M. Liao, Y. He, Q. Liu, J. Liu, H. Zhang, Z. Li and J. Wang, *Eur. J. Inorg. Chem.*, 2017, **2017**, 1143–1152.
- 16 G. Qu, B. Tian, C. Su, Y. Tang and Y. Li, *Chem. Commun.*, 2018, **54**, 10355–10358.
- 17 Q. Guan, J. Cheng, B. Wang, W. Ni, G. Gu, X. Li, L. Huang, G. Yang and F. Nie, *ACS Appl. Mater. Interfaces*, 2014, **6**, 7626–7632.
- 18 J. Hong, Y.-W. Lee, D. Ahn, S. Pak, J. Lee, A. R. Jang, S. Lee, B. Hou, Y. Cho, S. M. Morris, H. S. Shin, S. Cha, J. I. Sohn and J. M. Kim, *Nano Energy*, 2017, **39**, 337–345.
- 19 X. Bai, J. Liu, Q. Liu, R. Chen, X. Jing, B. Li and J. Wang, *Chem. – Eur. J.*, 2017, **23**, 14839–14847.
- 20 S. Zhang, D. Li, S. Chen, X. Yang, X. Zhao, Q. Zhao, S. Komarneni and D. Yang, *J. Mater. Chem. A*, 2017, **5**, 12453–12461.
- 21 E. Shangguan, L. Guo, F. Li, Q. Wang, J. Li, Q. Li, Z. Chang and X.-Z. Yuan, *J. Power Sources*, 2016, **327**, 187–195.
- 22 Y. X. Zeng, M. H. Yu, Y. Meng, P. P. Fang, X. H. Lu and Y. X. Tong, *Adv. Energy Mater.*, 2016, **6**, 17.

- 23 H. Wan, J. Liu, Y. Ruan, L. Lv, L. Peng, X. Ji, L. Miao and J. Jiang, *ACS Appl. Mater. Interfaces*, 2015, **7**, 15840–15847.
- 24 X. Cao, C. Tan, M. Sindoro and H. Zhang, *Chem. Soc. Rev.*, 2017, **46**, 2660–2677.
- 25 J. Sun, Y. Huang, C. Fu, Y. Huang, M. Zhu, X. Tao, C. Zhi and H. Hu, *J. Mater. Chem. A*, 2016, **4**, 14877–14883.
- 26 Y. Wang, Y. Song and Y. Xia, *Chem. Soc. Rev.*, 2016, **45**, 5925–5950.
- 27 H. Wang, Z. Xu, H. Yi, H. Wei, Z. Guo and X. Wang, *Nano Energy*, 2014, **7**, 86–96.
- 28 J. Yang, C. Yu, X. M. Fan, S. X. Liang, S. F. Li, H. W. Huang, Z. Ling, C. Hao and J. S. Qiu, *Energy Environ. Sci.*, 2016, **9**, 1299–1307.
- 29 W. K. Chee, H. N. Lim, Z. Zainal, N. M. Huang, I. Harrison and Y. Andou, *J. Phys. Chem. C*, 2016, **120**, 4153–4172.
- 30 X. Yu, Y. Kang and H. S. Park, *Carbon*, 2016, **101**, 49–56.
- 31 X. Y. Liu, Y. Q. Gao and G. W. Yang, *Nanoscale*, 2016, **8**, 4227–4235.
- 32 Z. B. Lei, J. T. Zhang, L. L. Zhang, N. A. Kumar and X. S. Zhao, *Energy Environ. Sci.*, 2016, **9**, 1891–1930.
- 33 M. Pang, G. Long, S. Jiang, Y. Ji, W. Han, B. Wang, X. Liu, Y. Xi, D. Wang and F. Xu, *Chem. Eng. J.*, 2015, **280**, 377–384.
- 34 J. Zhu, S. Tang, J. Wu, X. Shi, B. Zhu and X. Meng, *Adv. Energy Mater.*, 2017, **7**, 1601234.
- 35 B. Zhu, S. Tang, S. Vongehr, H. Xie, J. Zhu and X. Meng, *Chem. Commun.*, 2016, **52**, 2624–2627.
- 36 C. Chen, Y. Zhang, Y. Li, J. Dai, J. Song, Y. Yao, Y. Gong, I. Kierzewski, J. Xie and L. Hu, *Energy Environ. Sci.*, 2017, **10**, 538–545.
- 37 A. Shanmugavani and R. K. Selvan, *Electrochim. Acta*, 2016, **189**, 283–294.
- 38 J.-J. Li, M.-C. Liu, L.-B. Kong, D. Wang, Y.-M. Hu, W. Han and L. Kang, *RSC Adv.*, 2015, **5**, 41721–41728.
- 39 M. Tong, S. Liu, X. Zhang, T. Wu, H. Zhang, G. Wang, Y. Zhang, X. Zhu and H. Zhao, *J. Mater. Chem. A*, 2017, **5**, 9873–9881.
- 40 S. Yue, H. Tong, L. Lu, W. Tang, W. Bai, F. Jin, Q. Han, J. He, J. Liu and X. Zhang, *J. Mater. Chem. A*, 2017, **5**, 689–698.
- 41 G. Cao, L. Ximeng, R. Weina, L. Xin, C. Chuanwei and W. John, *Adv. Energy Mater.*, 2017, **7**, 1602391.
- 42 T. Xiao, P. Che, R. Xiao, P. Xiang, L. Jiang, F. Tao, X. Tan and X. Chen, *Appl. Surf. Sci.*, 2021, **543**, 148747.
- 43 C. V. V. M. Gopi, R. Vinodh, S. Sambasivam, I. M. Obaidat, S. Singh and H.-J. Kim, *Chem. Eng. J.*, 2020, **381**, 122640.
- 44 P. Rosaiah, J. H. Zhu, D. P. M. D. Shaik, O. M. Hussain, Y. J. Qiu and L. Zhao, *J. Electroanal. Chem.*, 2017, **794**, 78–85.
- 45 A.-A. M. Barmi, M. A. Moosavian, M. Aghazadeh and A. N. Golikand, *J. Mater. Sci.: Mater. Electron.*, 2020, **31**, 19569–19586.
- 46 Z. Song, W. Liu, W. Wei, C. Quan, N. Sun, Q. Zhou, G. Liu and X. Wen, *J. Alloys Compd.*, 2016, **685**, 355–363.